INTERFACE

royalsocietypublishing.org/journal/rsif

Research

Cite this article: Böddeker TJ, Karpitschka S, Kreis CT, Magdelaine Q, Bäumchen O. 2020 Dynamic force measurements on swimming *Chlamydomonas* cells using micropipette force sensors. *J. R. Soc. Interface* **17**: 20190580. http://dx.doi.org/10.1098/rsif.2019.0580

Received: 16 August 2019
Accepted: 10 December 2019

Subject Category:
Life Sciences–Physics interface

Subject Areas:
biophysics, biomechanics

Keywords:
microswimmers, *Chlamydomonas*, flagella, cell motility, force measurements, active matter

Author for correspondence:
Oliver Bäumchen
e-mail: oliver.baeumchen@ds.mpg.de

†Present address: Department of Materials, Eidgenössische Technische Hochschule (ETH) Zürich, Zürich, Switzerland.

Electronic supplementary material is available online at https://doi.org/10.6084/m9.figshare.c.4788711.

THE ROYAL SOCIETY PUBLISHING

Dynamic force measurements on swimming *Chlamydomonas* cells using micropipette force sensors

Thomas J. Böddeker†, Stefan Karpitschka, Christian T. Kreis, Quentin Magdelaine and Oliver Bäumchen

Max Planck Institute for Dynamics and Self-Organization (MPIDS), Am Faßberg 17, 37077 Göttingen, Germany

QM, 0000-0002-5705-8313; OB, 0000-0002-4879-0369

Flagella and cilia are cellular appendages that inherit essential functions of microbial life including sensing and navigating the environment. In order to propel a swimming microorganism they displace the surrounding fluid by means of periodic motions, while precisely timed modulations of their beating patterns enable the cell to steer towards or away from specific locations. Characterizing the dynamic forces, however, is challenging and typically relies on indirect experimental approaches. Here, we present direct *in vivo* measurements of the dynamic forces of motile *Chlamydomonas reinhardtii* cells in controlled environments. The experiments are based on partially aspirating a living microorganism at the tip of a micropipette force sensor and optically recording the micropipette's position fluctuations with high temporal and sub-pixel spatial resolution. Spectral signal analysis allows for isolating the cell-generated dynamic forces caused by the periodic motion of the flagella from background noise. We provide an analytic, elasto-hydrodynamic model for the micropipette force sensor and describe how to obtain the micropipette's full frequency response function from a dynamic force calibration. Using this approach, we measure the amplitude of the oscillatory forces during the swimming activity of individual *Chlamydomonas reinhardtii* cells of 26 ± 5 pN, resulting from the coordinated flagellar beating with a frequency of 49 ± 5 Hz. This dynamic micropipette force sensor technique generalizes the applicability of micropipettes as force sensors from static to dynamic force measurements, yielding a force sensitivity in the piconewton range. In addition to measurements in bulk liquid environment, we study the dynamic forces of the biflagellated microswimmer in the vicinity of a solid/liquid interface. As we gradually decrease the distance of the swimming microbe to the interface, we measure a significantly enhanced force transduction at distances larger than the maximum extent of the beating flagella, highlighting the importance of hydrodynamic interactions for scenarios in which flagellated microorganisms encounter surfaces.

1. Introduction

Microbial motility governs a variety of phenomena in microbiology, biophysics, as well as in many other fields of research, and has been studied intensively for decades [1,2]. The propulsion of bacteria, microalgae, nematodes and other single- and multicellular microorganisms in a liquid medium can be realized either by the periodic motion of cellular appendages such as flagella and cilia, as for single-flagellated spermatozoa and the multiflagellated model microbes *Escherichia coli* and *Chlamydomonas reinhardtii*, or by oscillatory shape changes, e.g. in case of the model nematode *Caenorhabditis elegans* [3]. Microbes exhibit rich dynamics in their motility patterns. The perception of gradients of, for example, chemicals, light intensity or fluid flow, may cause precisely timed modulations of the periodic motions of cellular appendages. In consequence, microbes

can navigate towards regions of high nutrient concentration (chemotaxis) [4,5], optimal light intensity (phototaxis) [6] or align relative to fluid flow (rheotaxis) [7]. The study of microbial motility in general, and the response of motile microbes to environmental cues in particular, calls for experimental methods allowing one to characterize the magnitude of the periodic forces underlying microbial propulsion. However, directly measuring the dynamic forces generated by cellular appendages of motile microbes is challenging due to the size of the organisms and the magnitude of the forces, which are often just a few micrometres and piconewtons, respectively. Moreover, measuring the forces generated by motile cells in their planktonic state, i.e. freely swimming in a liquid medium, demands experimental techniques that do not rely on supporting the cell by a substrate as in conventional atomic force microscopy approaches [8,9]. Ultimately, one wishes to quantify also the modulations of these forces due to environmental cues, which requires simultaneous access to chemical composition, light intensity, fluid flow and other relevant parameters in the vicinity of the swimming microorganism.

To date, experimental techniques for characterizing the swimming motility of microbes largely rely on optical measurements and on the trapping of self-propelled cells by optical tweezers [10–12]. *Chlamydomonas reinhardtii*, a unicellular, photoactive microalga with a cell diameter of about 8–10 µm featuring two anterior flagella, is a prime model organism in microbial motility studies. Measurements of its swimming dynamics have been carried out by tracking the cell body [13–17], particle imaging velocimetry (PIV) of the fluid around the organism [16,18,19], and by analysing the spatio-temporal changes of the flagella shape during its swimming strokes [13,15,18,20–24]. The main drawback of these methods is their indirect approach, requiring a model for the flagellar hydrodynamics, typically using slender-body and resistive force theory [25], to obtain estimates of the acting forces. Direct force measurements on *C. reinhardtii* have so far only been realized using optical tweezers [26]. This approach, however, is limited to the measurement of the maximum (escape) force per cell. Since biophysical techniques enabling truly direct force measurements are lacking to date, a conclusive picture of the mechanics and coordination of cilia and flagella, which control microbial motility, still remains elusive [27]. This includes an ongoing debate whether hydrodynamic or steric contact forces dominate the interaction of puller-type microswimmers with interfaces, as well as their impact on microbial navigation in confined spaces [28,29].

Attaching individual microorganisms to hollow glass micropipettes by applying a negative pressure on the inside of the pipette is a common technique to keep motile cells in the focal plane of a microscope to track the dynamics of their freely beating cilia or flagella [15,18,20–24]. In principle, forces can be measured simultaneously through the deflection of the micropipette. However, previous works using such micropipette force sensors [30–36] were limited to quasi-static measurements. In this case, the damping of the micropipette cantilever by hydrodynamic drag forces remains negligible, and forces can be directly recovered from the cantilever deflection and its spring constant. In the context of microbial propulsion, micropipette force sensors have been applied successfully to the millimetre-sized nematode *C. elegans* [37–39], which has a typical beating frequency of about 2 Hz only [37]. Many flagellated and ciliated microswimmers, however, operate at much higher frequencies. In addition, they generate forces that are smaller by about two to three orders of magnitude, compared to the reported nanonewton propulsion forces of *C. elegans*. Measurements of propulsion forces at higher frequencies have been impossible so far because hydrodynamic drag forces become significant in the frequency range of the cantilever actuation.

Here, we establish a novel force measurement method and, using this technique, present the first, direct measurements of the dynamic forces originating from the periodic flagella beating of a living microorganism. The centrepiece of the technique is a highly flexible, double-L-shaped micropipette, which serves as a calibrated dynamic force cantilever. An individual *C. reinhardtii* cell is attached to the tip of the micropipette such that forces exerted in the direction of its regular swimming motion are orthogonal to the cantilever arm (figure 1*a–c*). The pipette deflection is recorded optically with high spatial and temporal resolution. Note that the periodic, breast-stroke-like beating of the two flagella defines a beating plane, which is stationary in this configuration but rotates at frequencies around 1–3 Hz during free swimming, giving rise to helical trajectories [13]. We establish a versatile method for a full calibration of the micropipette's frequency response function and show that signal analysis in Fourier space allows for isolating the signal caused by the beating flagella of *C. reinhardtii* from external vibrations and background noise fluctuations. This novel experimental approach enables direct measurement of dynamic forces in the piconewton range, generated by flagellated cells at high frequencies. Simultaneously, important environmental control parameters can be accessed. We resolve the forces generated by the beating flagella of *C. reinhardtii* as a function of their distance to a solid interface, elucidating the nature of wall interaction mechanisms of puller-type microswimmers.

2. Experiments

2.1. Dynamic micropipette force sensors

The micropipette force sensor used to measure the dynamic forces exerted by the cell's flagella is custom-made, largely following the recipes for quasi-static force measurements [32]. A glass capillary tube is pulled asymmetrically to achieve a long tapered end. Using a microforge, the tapered micropipette is cut to size and bent twice by 90°, yielding the typical double-L shape shown in figure 1*a*. Alterations of the pulling speed and variations in the shaping of the cantilever allow us to adjust the nozzle size and cantilever stiffness. The force sensor is immersed in a liquid cell mounted on an inverted microscope, which is supported by an active vibration-cancelling table. By attaching a syringe to the pipette and placing it below the level of the liquid cell, i.e. by using a hydrostatic pressure difference, a motile *C. reinhardtii* cell can be partially aspirated at the tip of the micropipette force sensor. Both flagella beat freely in the liquid medium during all experiments (figure 1*b*).

2.2. Data acquisition

We now measure the oscillatory forces and flagella beating frequency of *C. reinhardtii* cells in bulk conditions. In order to extract the micropipette deflection during the microbe's swimming motion, we record the micropipette cross-section close to the nozzle with a 40× objective (figure 1*d*,*e*). A set of data consists of $N = 2^{15}$ cross-section images taken at $f_{\mathrm{sample}} = 400$

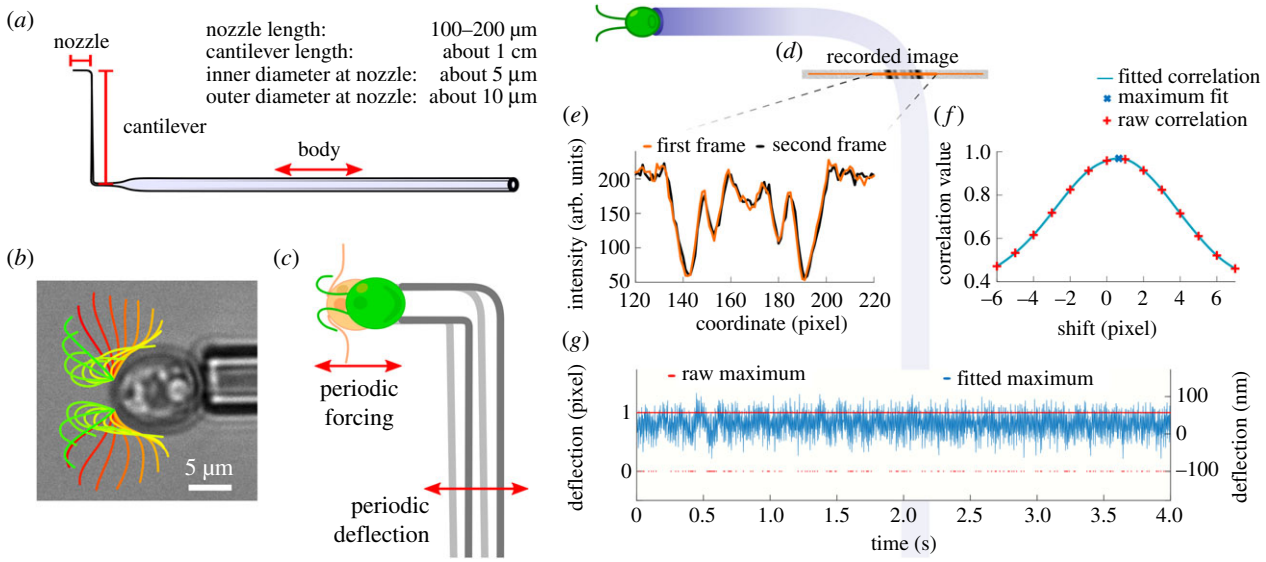

Figure 1. Dynamic force measurements on swimming *C. reinhardtii* cells using micropipette force sensors. (*a*) Sketch of the micropipette force sensor. (*b*) Micrograph of a swimming *C. reinhardtii* cell fixated at the tip of the nozzle overlaid with the flagella shapes throughout one beating cycle. Time is colour coded from red to green. The time step between snapshots is 1.55 ms, corresponding to a flagella beating frequency of about 46 Hz. The original movie is provided as electronic supplementary material, movie. (*c*) The cell is held at the nozzle of the micropipette and exerts a periodic forcing that leads to a periodic deflection of the cantilever. (*d*) Exemplar micrograph of the pipette cross-section recorded at the end of the cantilever. (*e*) Intensity profiles of two subsequent cross-section images. (*f*) Correlation analysis of two frames to determine the relative shift corresponding to the maximal correlation. Interpolating the discrete correlation function results in sub-pixel deflection resolution. (*g*) Discrete and sub-pixel micropipette deflection over time. The pixel size is 0.16 µm per pixel.

frames per second (fps), resulting in an observation time of about 82 s. We determine the micropipette's deflection for any given frame as the shift of the current pipette position relative to the pipette position in the first frame using a cross-correlation analysis of the intensity profiles of the pipette cross-section, see figure 1*f*, following established protocols [30,32]. Determining the micropipette position as precisely as possible is crucial for the accuracy of the dynamic force measurement. We find that the pixel-wise correlation analysis, where the maximal correlation alternates between two pixels, does not result in a sufficient spatial resolution and introduces an error in the force measurements. Interpolating the correlation curve and extracting the shift corresponding to the maximum of the interpolation, however, reveals a fluctuating signal with sub-pixel resolution (figure 1*g*).

2.3. Microbial propulsion in the context of Fourier analysis

While the micropipette deflections with and without a cell attached appear similar in real space, see figure 2*a*,*b*, a distinct signal originating from the oscillatory forcing of the flagella can be identified in the frequency domain, as seen in figure 2*c*. Conceptually, it is important to distinguish between periodic forcing and the mean propulsion force generated by the beating flagella. In order to propel itself, a microswimmer must generate a positive mean force during one beat cycle of its flagella. Sustained propulsion requires periodic motion of the flagella. The instantaneous forcing exerted by a swimming microbe can, consequently, be decomposed into a constant and an oscillating force. A minimal model of microbial propulsion, consisting of a sinusoidal forcing with non-zero mean, i.e. with a constant offset, is illustrated in electronic supplementary material, figure S1. Decomposition of the instantaneous forcing into components of different frequency through Fourier analysis allows the mean force and the periodic force to be distinguished. In the frequency domain, the constant mean force results in a peak at zero frequency. In our measurement configuration, this corresponds to a constant offset in the pipette deflection. Since we only record the pipette deflection relative to the first frame, we cannot access the mean force with this technique. The mean propulsion force has, however, already been calculated by recording the swimming velocity of a single cell and applying Stokes drag [14]. The oscillatory component of the instantaneous forcing, on the other hand, leads to a distinct signature in the frequency domain as shown in figure 2*c*.

2.4. Signal analysis of the pipette deflection

The single-sided power spectrum (normalized squared Fourier coefficients, abbreviated as PSD) of the micropipette fluctuations displays a clear cell signal in the frequency range between 50 and 65 Hz, which agrees well with the typical flagella beating frequency of *C. reinhardtii* [13]. This signal disappears once the cell is released from the micropipette nozzle. The PSD is calculated as

$$\mathrm{PSD}_j = N \cdot X_j^2, \tag{2.1}$$

where the discrete Fourier coefficients X_j of an N-pointed array x_n are defined as

$$X_j = \sum_{n=0}^{N-1} x_n \, \mathrm{e}^{-2\pi \mathrm{i} jn/N}, \tag{2.2}$$

for $j = 0, 1, \ldots, N-1$.

Note that despite the fact that all experiments were performed using an active vibration-cancelling table, the full power spectrum may still show signatures of building vibrations at low frequencies and/or electrical devices (e.g. camera fans) at high frequencies. Spectra over the full frequency range of the measurement in figure 2*c* are shown in

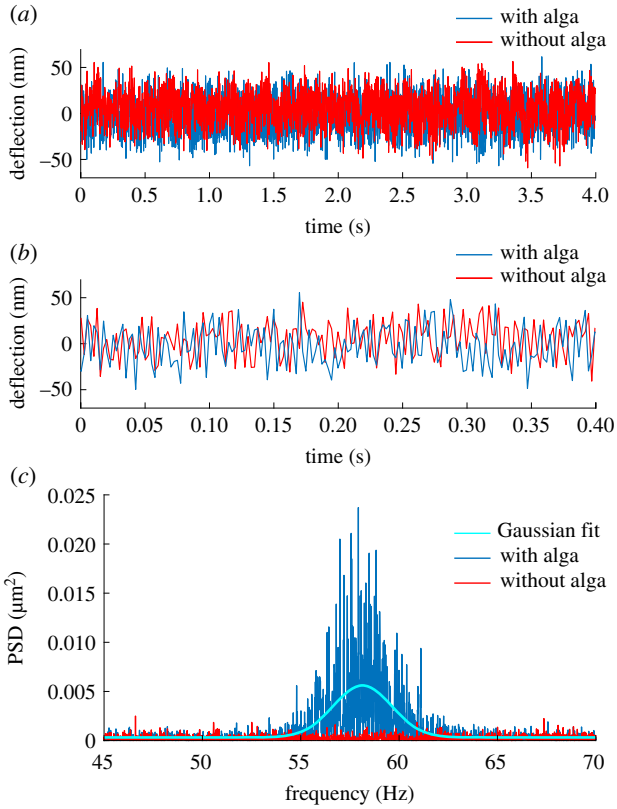

Figure 2. Force sensor signal analysis. (*a*) Section of a representative micropipette deflection with and without a cell attached (total recording time of the experiment was 82 s). (*b*) Zoomed deflection with and without alga. (*c*) Power spectra of the experimental deflection data of which sections are shown in (*a*) and (*b*). The power spectrum of the deflection with a cell attached (blue) reveals a distinct signal between 55 and 60 Hz, whereas the power spectrum of the same micropipette without a cell attached (red) shows only noise. The solid line represents a Gaussian fit to the cell signal.

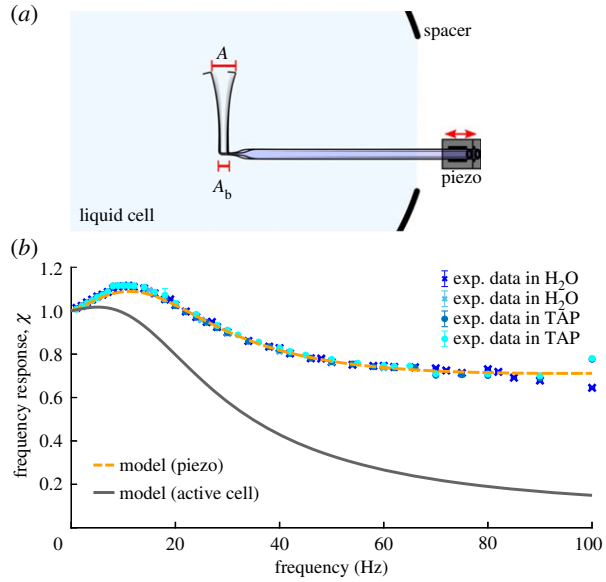

Figure 3. Dynamic calibration. (*a*) Set-up and relevant parameters for the experimental calibration of the frequency response $\chi = A/A_0$. In the calibration case, the static response $A_0 = A_b$ is given as the amplitude of the sinusoidal motion of the pipette base prescribed by the piezo. (*b*) Frequency response χ of the micropipette force sensor for the calibration and measurement configuration. Experimental calibration data (symbols) and the theoretical model (dashed line) fitted to the experimental results validate the applicability of the theory and allow for calculating the frequency response for boundary conditions during measurements with an active cell (solid line). We also find that the differences in viscosity and density of water (H_2O, typical calibration liquid) and tris-acetate-phosphate (TAP) cell medium can be safely neglected in the frequency response.

electronic supplementary material, figure S2. Since none of these external signals fall into the frequency range associated with the flagella beating, they do not interfere with the signal originating from the cell in Fourier space. The beating frequency f of the flagella fluctuates over time and the frequency distribution may well be described by a Gaussian distribution [23]; thus, we use a Gaussian fit to extract the cell signal and isolate it from external noise (figure 2*c*). The fit function of the Gaussian distribution is defined as

$$g(f) = a \cdot \exp\left(-\frac{(f-\mu)^2}{2\sigma^2}\right) + d, \tag{2.3}$$

with amplitude a, mean beating frequency μ, variance σ and constant offset d. By subtracting the offset from the fit, we eliminate the white noise contribution from the power spectrum. Using Parseval's theorem, we can also extract the signal power associated with the oscillatory beating of the flagella P'_c as the area of the Gaussian curve minus the offset:

$$P'_c = \frac{\sqrt{2\pi}\sigma a}{\Delta f}, \tag{2.4}$$

with binning width of the discrete Fourier transform $\Delta f = f_{sample}/N$. The associated error of P'_c is calculated using error propagation of the uncertainties of the fit parameters σ and a. Note that the power spectrum, along with P'_c, is given in units of squared deflection, since we have not yet taken into account the frequency response and spring constant of the micropipette cantilever.

2.5. Dynamic force calibration

In order to convert the pipette fluctuations into forces, the micropipette force sensor has to be calibrated. For static and quasi-static force measurements, i.e. at low frequencies of at most a few hertz, it suffices to determine the micropipette's spring constant k. We measured k by recording the pipette deflection caused by the changing weight of an evaporating water droplet attached to the tip of the micropipette [30,32]. Typical spring constants of the pipettes used in our experiments are around 1 nN μm^{-1}. Performing measurements on the dynamics of cellular appendages at high frequencies also requires a full characterization of the micropipette's frequency response χ. An oscillatory force of a given frequency acting upon the cantilever results in a deflection with amplitude A. The frequency response is then generally defined as $\chi = A/A_0$, with amplitude A_0 caused by a static force of equal magnitude. Determining the frequency response under the exact same conditions found throughout an experiment, i.e. with an oscillating forcing applied to the pipette nozzle and a stationary micropipette base, is experimentally challenging. We quantify the frequency response under more accessible boundary conditions, where the micropipette is actuated inside the liquid cell with a sinusoidal motion at its clamped body by a closed-loop piezo actuator, as shown in figure 3*a*. The experimental calibration data can then be translated into the response for the boundary conditions found throughout experiments with an active

cell using the theoretical model outlined in §3. In brief, we model the micropipette force sensor as a tapered, hollow elastic beam that is oscillating in a viscous liquid. The dynamical deflection of the pipette is described with the Kirchhoff equations, coupled to the time-dependent Stokes equations to take viscous and inertial fluid drag into account [40]. Inertia and hydrodynamic drag of the nozzle are implemented as a localized dynamic loading at the end of the elastic beam. In the model, the boundary conditions found throughout the measurements on active cells correspond to a concentrated time-dependent loading at the tip of a cantilever, while the body of the micropipette is stationary. The calibration measurements correspond to a free tip and a clamped body that is oscillating in normal direction.

Figure 3*b* shows the frequency response χ of the micropipette, normalized to the static response. For calibration boundary conditions, i.e. actuation with a piezo, experimental (symbols) and theoretical (dashed line) results are in excellent agreement. For the boundary conditions of experiments with an active cell, we calculate the corresponding response of the micropipette cantilever (figure 3*b*, solid line). The error of the response curve is estimated by the mean deviation between the experimental and model calibration data and translated to the active cell case as a relative error.

3. Elasto-hydrodynamic model

In order to model the oscillation of the micropipette in a liquid medium, we simplify the pipette geometry, treating the cantilever part as a straight, tapered beam that is oscillating at small amplitude normal to its long axis. The nozzle of the pipette is treated as a long, thin rod that is oscillating in longitudinal direction. Inertial and drag forces from the nozzle are then coupled to the cantilever as a concentrated load at the cantilever's end, together with the forces generated by attached cells. To model the cantilever motion, we closely follow the approach by Sader [40], using the Kirchhoff equation for a tapered beam:

$$\frac{\partial^2}{\partial x^2}\left(B(x)\frac{\partial^2 w(x,t)}{\partial x^2}\right)+m(x)\frac{\partial^2 w(x,t)}{\partial t^2}=\mathcal{F}(x,t). \tag{3.1}$$

Here, $x\in[0,L]$ is the coordinate along the cantilever of length L and w is the displacement of the cantilever from its resting position perpendicular to its long axis.

$$B(x)=\frac{\pi}{4}E(R(x)^4-r(x)^4) \tag{3.2}$$

and

$$m(x)=\pi\rho_p(R(x)^2-r(x)^2)+\pi\rho\, r(x)^2 \tag{3.3}$$

are bending modulus and mass per unit length of the tapered cantilever, respectively. E and ρ_p are Young's modulus and density of the pipette material, r and R are inner and outer radius, respectively, and ρ is the density of the medium inside the pipette. $\mathcal{F}(x,t)$ is the spatio-temporal loading distributed along the cantilever, which is given by viscous and inertial drag of the surrounding fluid medium. The spring constant k can be derived from the static version of equation (3.1), which is obtained by setting $\partial w(x,t)/\partial t\equiv 0$ and $\mathcal{F}(x,t)\equiv 0$.

In order to quantify the hydrodynamic drag in the dynamic case, we first analyse the relevant length scales in the problem. These are the amplitude of the oscillation, $A\sim 0.1$ µm, the outer diameter of the pipette, $2R\sim 50$ µm, and the thickness of the viscous boundary layer $\lambda=\sqrt{2\eta/\rho\omega}\sim 70$ µm, where η is the viscosity of the medium and $\omega=2\pi f$ is the angular frequency of the oscillation. In our case, $A\ll R\sim\lambda$, which is a small amplitude oscillation in a viscous medium. We define the Reynolds number for the local acceleration term,

$$Re=\rho\omega R^2/\eta\sim 0.2, \tag{3.4}$$

and, accordingly, describe the fluid velocity u and pressure p by the time-dependent Stokes equation [40,42],

$$\rho\frac{\partial u}{\partial t}=-\nabla p+\eta\nabla^2 u, \tag{3.5}$$

supplemented by the continuity equation for an incompressible fluid, $\nabla\cdot u=0$, a no-slip boundary condition at the surface of the cantilever, and require a quiescent fluid at large distance. Solving the fluid mechanics problem for the actual shape of the cantilever would require full numerical simulations, coupled to equation (3.1). However, the taper angle of the cantilever is very small and it can locally be approximated by a cylindrical beam, for which analytical solutions to the time-dependent Stokes equation exist.

Due to the linearity of equations (3.1) and (3.5), they are best solved after Fourier-transformation with respect to time, yielding

$$\frac{\mathrm{d}^2}{\mathrm{d}x^2}\left(B(x)\,\frac{\mathrm{d}^2\hat{w}(x)}{\mathrm{d}x^2}\right)-m(x)\omega^2\hat{w}(x)=\hat{\mathcal{F}}(x) \tag{3.6}$$

and

$$-i\rho\omega\hat{u}=-\nabla\hat{p}+\eta\nabla^2\hat{u}, \tag{3.7}$$

in which the '^' indicates transformed quantities and the angular frequency ω merely acts as a parameter [40]. The solution of the time-dependent Stokes equation is a lengthy derivation that can be found in [43]. Here, we repeat the resulting net load per unit length onto the cantilever [40]:

$$\hat{\mathcal{F}}(x)=\pi\rho\,\omega^2 R(x)^2\Gamma(x,\omega)\,\hat{w}(x), \tag{3.8}$$

with the hydrodynamic function $\Gamma(\omega)$ that reads, for oscillation perpendicular to the long axis [40],

$$\Gamma(x,\omega)=1+\frac{4iK_1(-i\sqrt{iRe})}{\sqrt{iRe}K_0(-i\sqrt{iRe})}, \tag{3.9}$$

where K_n are the modified Bessel functions of the second kind and n-th order. Note that in this formulation, Γ and Re have to be evaluated for the local cross-section and, for a tapered beam, thus depend on x.

The boundary conditions are an external load F that, together with the hydrodynamic drag of the nozzle, is concentrated at $x=L$. We approximate the nozzle as a long, thin cylinder of radius $R(L)$ and length L_n, and thus describe it by the solution to the axisymmetric version of Stokes' second problem [43]. The boundary condition at $x=L$ is

$$\begin{aligned}-\frac{\partial}{\partial x}\left(B(x)\frac{\partial_x^2\hat{w}(x)}{\partial x^2}\right)\Big|_{x=L}&=\hat{F}\\ -L_n(\pi\rho R(L)^2\Gamma_n(\omega)+m(L))\omega^2\,\hat{w}(L)&\end{aligned} \tag{3.10}$$

and

$$\hat{w}''(L)=0, \tag{3.11}$$

where $\Gamma_n(\omega)=(\Gamma^*(L,\omega)-1)/2$ is the hydrodynamic function for a long cylinder in axial oscillation and '*' denotes conjugation. At the clamped end of the beam at $x=0$, an oscillation with angular frequency ω and amplitude w_0

is prescribed:

$$\hat{w}(0) = w_0 \quad \text{and} \quad \hat{w}'(0) = 0. \tag{3.12}$$

In calibration conditions, $\hat{F} = 0$ and $w_0 \neq 0$; in measurement conditions, $\hat{F} \neq 0$ and $w_0 = 0$. With these boundary conditions, equation (3.6) is solved numerically to obtain the spring constant and resonance curves. Since the resonance curves strongly depend on the pipette geometry, we allow for global additive corrections to the measured geometry parameters, $r(x) + \delta r$, $R(x) + \delta R$, $L + \delta L$ and $L_n + \delta L_n$, that are obtained by fitting the resonance curve to the experimental calibration data. Fitting is performed by a finite differencing scheme of the numerical resonance curves. Importantly, the correction values are constrained to be within the uncertainty of the respective measurements of the pipette geometry. A representative measurement of the pipette geometry is illustrated in electronic supplementary material, figure S3. δr, δR and δL must fulfil an additional relation that matches the spring constant in the model to the experimentally determined one using the added weight of an evaporating water droplet. The resulting correction values are below 1 µm for the radii and of the order of 10 µm for the lengths. We provide a Mathematica script as electronic supplementary material, code, that demonstrates the numerical solution of the equations above to obtain the calibration and measurement resonance curves displayed in figure 3*b*.

4. Results

The final step of the analysis is the conversion of the signal power P'_c, see equation (2.4), to physical quantities using the dynamic force calibration outlined above. Note that an inverse Fourier transform does not suffice to recover the motion of the flagella. We have lost the information about the phase throughout the signal analysis by squaring all coefficients to calculate the power spectrum and by fitting the signal with a Gaussian in order to eliminate noise. Instead, we perform a manual inverse Fourier transform by projecting the signal power P'_c into a single sinusoidal with frequency μ to recover the periodic forcing $F_o(t)$, using

$$F_o(t) = \sqrt{\frac{2P'_c}{N}} \cdot \frac{k}{\chi(\mu)} \sin(2\pi\mu t), \tag{4.1}$$

with amplitude F_o, spring constant k and frequency response $\chi(\mu)$. N in the prefactor is the number of data points in the transform and accounts for a correct normalization of the power spectrum according to the Fourier transform defined in equation (2.2). The factor 2 originates from the normalization of the power spectrum of a sinusoidal signal. The error of F_o is calculated using error propagation of individual errors of P'_c, k and $\chi(\mu)$, where the error of k is taken as the standard deviation of all experimental spring constant calibrations for a given micropipette.

Overall 112 individual measurements with nine different cells were performed in bulk. The experiments yielded a mean amplitude of the periodic forcing of 26 pN with a standard deviation of 5 pN and a mean beating frequency of 49 Hz with a standard deviation of 5 Hz. Histograms of the mean beating frequency μ and mean oscillatory force F_o of nine different cells (at least two measurements per cell) and of 42 measurements of the same cell recorded over a time period of more than two hours are shown in figure 4*a–c*, respectively. Cell–cell variations and variations of the dynamic forces of a single cell over time are larger than the error of individual force measurements (1.8 pN on average).

In the following, we extend our experiments towards dynamic force measurements on living *C. reinhardtii* cells in the vicinity of a solid wall in order to study the effect of flagella/wall interactions and, in particular, characterize the presence and magnitude of hydrodynamic interactions between beating flagella and the surface of the wall. Figure 4*d* displays three representative PSDs for the exact same cell, recorded at different distance z between the cell body and the surface of a silicon wafer. The experimental set-up and orientation of the cell relative to the interface are shown in electronic supplementary material, figure S4. For $z = 4.6$ µm, we find a lowered mean beating frequency μ as compared to the PSD recorded at $z = 16.3$ µm, which can be safely considered bulk swimming. Besides the shift of the mean frequency, also the variance of the frequency σ is found to increase substantially, which indicates that steric interactions alter the regular beating pattern near the interface. Interestingly, already at intermediate distances, i.e. $z = 9.1$ µm, the signature of the flagella beating in the PSD differs significantly from the bulk measurement, as shown in the inset of figure 4*d*. This is a first indication that hydrodynamic interactions might indeed be detectable in recorded cell signals, given that the flagella of *C. reinhardtii* only have a maximal forward reach of 7 to 8 µm in the unperturbed beating pattern (figure 1*b*).

We studied overall 8 different cells at varying distance z between the base of the flagella and the wall and recorded the respective amplitudes of the dynamic forces F_o following the approach outlined in the previous sections and equation (4.1). Note that we normalize F_o of a given cell by the respective value in bulk conditions to account for cell–cell variations. Based on our results, we consider the experimental data recorded at distances over 15 µm from the wall as bulk measurements. The data for F_o/F_{bulk} are shown in figure 4*e*, while the inset displays the corresponding normalized variance σ/σ_{bulk} of the flagella beating frequencies in the PSD. Significant deviations of the forcing from the bulk values occur at distances smaller than about 12 µm from the wall. Below this threshold, we find a monotonic increase of the normalized dynamic force F_o/F_{bulk} for decreasing distance of the cell body to the wall. The fact that the dynamic forcing is already significantly enhanced at distances greater than the maximal flagella forward reach of 7 to 8 µm, e.g. we find $F_o = 42.1 \pm 3.0$ pN at $z = 9.1$ µm when compared with $F_o = 23.9 \pm 1.9$ pN in bulk for the datasets shown in figure 4*d*, strongly suggests an effect of hydrodynamic interactions. In the regime below distances of 7 to 8 µm, we expect steric interactions between the flagella and the wall to dominate, in line with the finding that the force transduction is further enhanced ($F_o = 60.6 \pm 4.2$ pN for the datasets shown in figure 4*d*). As shown in the inset of figure 4*e*, the normalized variance of the beating frequency σ/σ_{bulk} abruptly increases at distances of 7 to 8 µm to the wall, which we attribute to flagella desynchronization due to transient flagella–substrate contact during every beating cycle. Thus, σ/σ_{bulk} as a function of the distance confirms the determination of the maximum forward reach of the flagella from the beating pattern.

5. Discussion

We established a direct experimental approach based on a dynamic micropipette force sensor (DMFS) for precise and robust measurements of the dynamic forces generated by

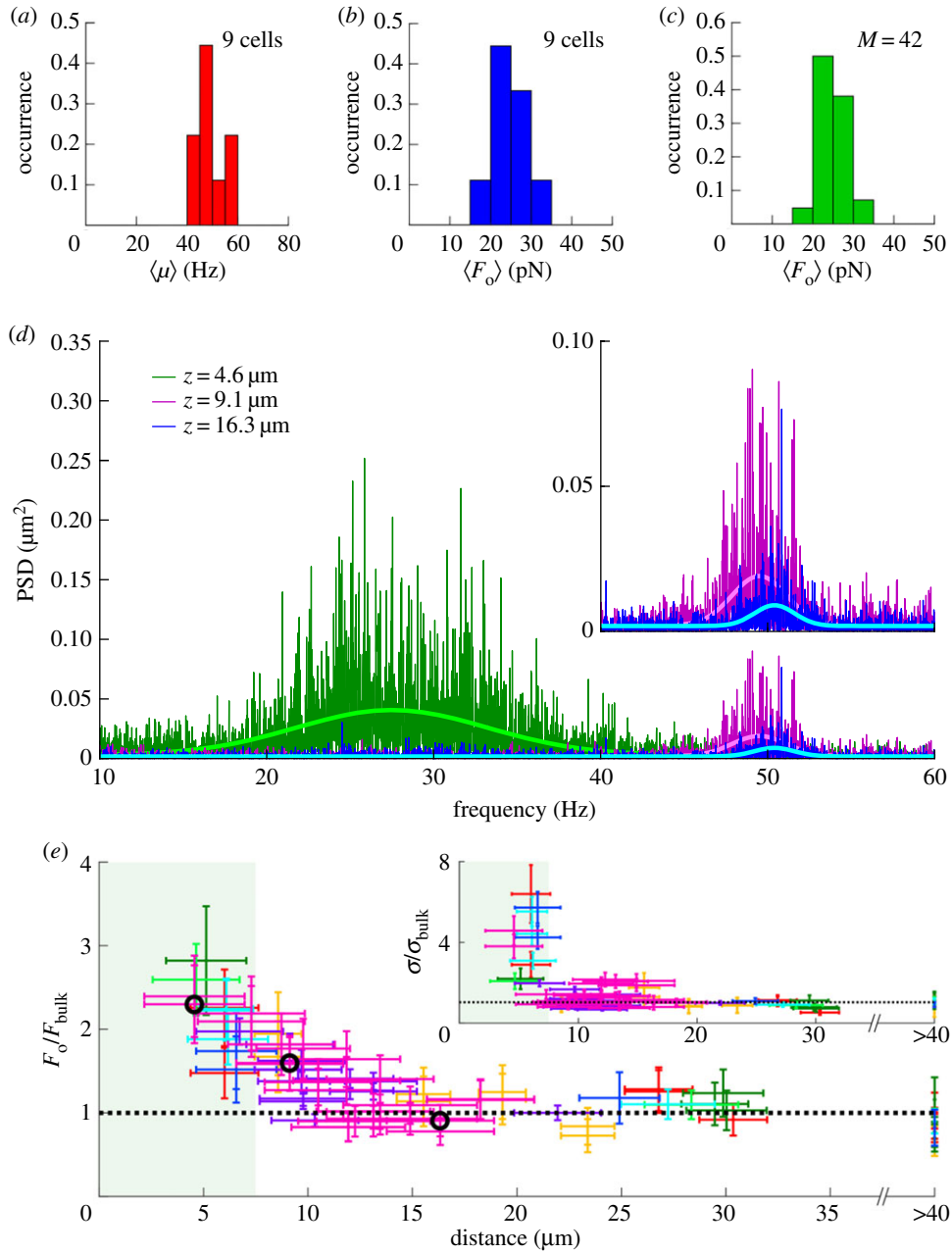

Figure 4. Dynamic force measurements on *C. reinhardtii* cells in bulk liquid and in proximity to a solid/liquid interface. (*a*) Distribution of mean values of the beating frequency μ for nine different cells recorded in bulk. (*b*) Distribution of mean values of the amplitude of the oscillatory force F_o for nine different cells recorded in bulk. (*c*) Distribution of F_o from $M = 42$ measurements in bulk for the same cell. (*d*) PSDs of the same cell at distance $z = 4.6$ µm (green, $\mu = 27.5$ Hz, $F_o = 60.6 \pm 4.2$ pN), at $z = 9.1$ µm (purple, $\mu = 49.5$ Hz, $F_o = 42.1 \pm 3.0$ pN) and at $z = 16.3$ µm (blue, $\mu = 50.4$ Hz, $F_o = 23.9 \pm 1.9$ pN) from the wall. (*e*) F_o as a function of distance z from the wall for eight different cells normalized by their respective bulk values F_{bulk} (dashed line). Data corresponding to different cells are distinguished by different colours. Open circles indicate the datasets displayed in (*d*). During unperturbed swimming, the flagella have a maximal forward reach of about 7–8 µm (figure 1*b*). The area shaded in green between 0 and 7.5 µm thus represents distances at which both flagella may experience steric interactions at the interface. The inset displays the corresponding normalized variance σ/σ_{bulk} of the cell signals in the PSD.

periodically beating cellular appendages at high frequencies. The observed mean beating frequency of *C. reinhardtii* of 49 ± 5 Hz falls into the expected range of beating frequencies from 40 to 64 Hz [13] and matches very well the previously reported mean beating frequency of 53 ± 5 Hz from high-speed cell tracking [16]. Our *in vivo* force measurements on *C. reinhardtii* yielded a mean amplitude of the periodic forcing of 26 ± 5 pN provided by the coordinated beating of both flagella. Assuming a sinusoidal functional form of the oscillatory forcing and adding the mean propulsion force as a constant offset, we can construct a minimal model of the instantaneous forcing throughout one beating cycle (see electronic supplementary material, figure S1). By extracting the swimming velocity from cell tracks and applying Stokes drag, the mean propulsion force of *C. reinhardtii* has been estimated to be 8 ± 2 pN [14], which, added to the oscillatory force, results in a maximum forcing of 34 ± 7 pN during one beating cycle. This value is in quantitative agreement with the measured escape forces of 26 to 31 pN of *C. reinhardtii* in optical tweezer experiments [26]. Assuming sinusoidal forcing, our dynamic force measurements yield that 40% [34 44] (square brackets indicate lowest and highest error bounds) of the beating cycle show negative instantaneous forces, i.e. correspond to the recovery stroke of the beating flagella, which is in accordance with previous

calculations of the instantaneous cell body speed [16] as well as hydrodynamic simulations [41].

In conclusion, we provided the first direct measurements of the dynamic forces of swimming microorganisms originating from the beating of their flagella, in varying environmental conditions. We established our experimental approach for *C. reinhardtii* cells in bulk liquid swimming conditions. With this approach, we measured the dynamic forces exerted by a pair of beating flagella in the vicinity of a solid surface.

The natural habitats of many microorganisms, including soil-dwelling *C. reinhardtii* microalgae, are confined spaces. Consequently, their navigation and motility are governed by frequent interactions with the confining walls. By characterizing the nature of the interactions of flagellated puller-type microbes encountering surfaces quantitatively, we are able to gain new insights regarding the microbial motility in complex natural and physiological environments. We find a gradual increase of the dynamic force transduction as we decrease the flagella–wall distance, well before steric contact interactions might take over, and attribute this regime to the presence of hydrodynamic interactions. This finding is relevant far beyond the microbial domain since eukaryotic flagella are well-preserved phenotypical features that exist in virtually all eukaryotic life forms, including the human body.

On the methodological side, we developed a novel experimental approach for direct dynamic force measurements with piconewton resolution, extending the applicability of micropipette force sensors from quasi-static to dynamic force measurements. The provided calibration protocol for determining the full frequency response function of the force sensor ultimately enables these quantitative dynamic force measurements. Under controlled experimental conditions, the DMFS method allows for extracting periodic forces from the power spectrum of the micropipette deflection data, after isolating the signal from background noise. The force measurements are based on the optical readout of the micropipette deflection with sub-pixel resolution, yielding a force sensitivity in the range of a few piconewtons.

The experimental technique is highly versatile and allows one to vary physiologically relevant parameters, such as illumination, exposure to drugs, external flow, and proximity to interfaces, even during on-going measurements. In combination with the ability to perform repeated measurements per cell over extended periods of time, DMFS appears as a unique tool to systematically quantify the effect of these parameters on microbial propulsion and the activity of cellular appendages. In the future, the full optical access to the biological sample may allow for simultaneously combining dynamic force measurements with flagella tracking, PIV measurements as well as contrast-enhanced optical techniques to observe the biological processes at work. Since DMFS can be readily implemented into existing experimental setups and by using tailored micropipette force sensors with customized geometry and sensitivity, we expect that in the future DMFS can be employed to measure dynamic forces of a variety of living systems, including microorganisms of different size and shape. Moreover, modifying the geometry of the micropipette cantilever could be employed to measure forces orthogonal to the direction of propulsion. Adjusting the orientation of the cell with respect to a substrate, e.g. such that the flagella beat parallel rather than orthogonal to the interface, could reveal an angular dependence of the force transduction for microbial wall encounters. In the light of these possible future research directions, we anticipate DMFS to be a valuable tool to not only study the propulsion of single- and biflagellated microorganisms, but also to open up new possibilities to quantify dynamic forces in multi-flagellated systems and multicellular colonies including, for example, species of the genus *Volvox* that feature hundreds or even thousands of beating cilia.

6. Material and methods

6.1. Cell cultivation

All experiments have been performed with wild-type *Chlamydomonas reinhardtii* strain SAG 11-32b. Axenic cell cultures were grown in tris-acetate-phosphate (TAP) medium (reference number A13798-01, Thermo Fisher Scientific, USA) on a 12 : 12 h day–night cycle in a Memmert IPP 100Plus incubator (Memmert, Germany). The daytime temperature was set to 24°C with a light intensity of 1 to 2×10^{20} photons $m^{-2}\,s^{-1}$. During the night cycle, the light intensity was zero and the temperature was reduced to 22°C. Experiments have been performed during the daytime with vegetative cells in the logarithmic growth phase on the 2nd to 4th day after incubation. Cells were suspended in a liquid cell filled with TAP under ambient laboratory conditions.

6.2. Micropipette fabrication and calibration consistency checks

The micropipette cantilevers were custom-made and adjusted in size and stiffness. A blank glass capillary (TW100-6, World Precision Instruments, USA, outer diameter 1 mm, inner diameter 0.75 mm) was pulled to the desired diameter using a micropipette puller (P-97, Sutter Instruments, USA). During the pipette pulling process, one side of the capillary was held stationary, while the other side was slowly pulled away. This yielded one short and one long, tapered pipette. Using a microforge (MF-900, Narishige Group, Japan), the long pipette was cut to the desired length and bent twice to achieve the desired shape. The bent pipette was finally filled with deionized water and placed in a water bath for storage. To modulate the suction pressure during experiments, the pipette was furnished with a water-filled tube attached to a syringe. As shown in electronic supplementary material, figure S3, the geometric dimensions of the micropipette force sensors were extracted from micrographs taken along the cantilever arm and nozzle. Subsequently, the measurements of inner and outer diameter were fitted with a second-order polynomial. All data presented here have been recorded with two pipettes, both of which have been calibrated individually. The experimentally measured spring constants determined using the evaporating-droplet method were $k_1 = 1.24 \pm 0.04$ nN µm^{-1} and $k_2 = 0.51 \pm 0.03$ nN µm^{-1}, where the error is given as the standard deviation of all measurements for a single pipette. The length of the pipettes were $L_1 = 11.2 \pm 0.3$ mm and $L_2 = 8.2 \pm 0.3$ mm, respectively. The outer diameter at the cantilever base and tip were $2R_1(x = 0) = 29.7 \pm 2$ µm, $2R_1(x = L) = 12.4 \pm 2$ µm, $2R_2(x = 0) = 19.5 \pm 2$ µm and $2R_2(x = L) = 8.6 \pm 2$ µm. Errors are estimated from the uncertainty of the optical measurement. Both Young's modulus E and density of the pipette glass ρ_p have been taken from the manufacturer's data.

We performed consistency checks to verify the experimental method used to determine the frequency response of the micropipette force sensor. Electronic supplementary material, figure S5, shows the frequency response of the force sensor under different amplitudes of the external forcing A_b. The frequency response $\chi = A/A_b$ was found to be independent of the amplitude within the range of applied amplitudes of up to 10 µm, which is about two orders larger than the pipette deflection found in the experiments with cells. To quantify the effect of the viscosity η of the liquid surrounding the pipette on the frequency response, we

performed the calibration in water and in a mixture of water and glycerol with approximately 3.5 times the viscosity of water. As expected for increased hydrodynamic drag, the damping increased in the latter case. The difference in viscosity of distilled water and TAP growth medium, however, was found to have a negligible effect on the micropipette's frequency response, as shown in figure 3*b*.

6.3. Experimental procedure

Experiments were performed in a liquid cell consisting of two glass slides (2947-75x50, Corning, USA) held in place by custom-made frames. Two spacers cut from an o-ring of 3 mm thickness and an inner diameter of 3.8 cm defined the experimental chamber. The glass slides were cleaned with ethanol (Uvasol, Merck, Germany) and completely dried before assembling the cell. The o-rings were also cleaned with ethanol, rinsed with water and then dried. The assembled cell was filled with TAP growth medium and mounted on an inverted microscope (IX83, Olympus, Japan). Liquid *C. reinhardtii* culture was injected into the cell. The culture was not centrifuged before injection but taken directly out of the liquid cultures in the incubator. The amount of cell culture injected into the liquid cell was adjusted such that a sufficient amount of *C. reinhardtii* were found in the chamber.

A thin slab of silicon cut from a wafer (type P/Bor, orientation 100, unilateral polished, Si-Mat, Germany) was glued onto a custom-made stainless steel substrate holder using polydimethylsiloxane (Dow Corning, USA). Substrate and holder were prepared for experiments by sonication in an ethanol bath and subsequent blow-drying with an air gun. The substrate was mounted onto a linear stage (M462 series, Newport Corporation, USA) capable of computer-controlled movement within the focal plane and mechanical adjustment of the height and pitch. The substrate was then inserted into the liquid cell and moved to the focal point of the microscope. Due to the phototaxis of *C. reinhardtii*, the cells can be guided towards the substrate in the light beam focused on the substrate. Under white light conditions, the flagella stick to surfaces such that the cells accumulate on the substrate [30,33]. The micropipette cantilever, furnished with a tube and syringe filled with deionized water, was mounted onto a 3-axis piezo-driven manual micromanipulator (PCS-5400, Burleigh, Thorlabs, USA) and inserted into the liquid cell. The substrate was then adjusted such that the surface was orthogonal to the pipette nozzle. An individual cell adhering to the substrate was approached by the pipette and fixated at the pipette nozzle with a suction pressure adjusted manually with the syringe. The fixated cell could then be detached from the substrate by retracting the pipette. Since only the flagella stick to the substrate [30], cells pulled off the substrate were oriented such that the flagella faced away from the pipette. Thus, the direction of the propulsion forces was orthogonal to the cantilever arm and the flagella were beating freely. Note that the flagella were not damaged when pulled off the substrate and recovered their regular beating pattern within tens of seconds [30]. For measurements in bulk conditions, the substrate was typically retracted for more than one millimetre from the pipette. In red light, the flagella-mediated adhesion of *C. reinhardtii* to substrates is inhibited [30], thus enabling one to probe the steric interactions between flagella and substrate. Measurements during which the flagella, even just transiently, attached to the substrate were discarded. In order to ensure comparability between bulk measurements and measurements in the proximity of the interface, a 550 nm cut-off filter was inserted into the light path for all experiments. The aperture of the microscope was completely opened during experiments and the light intensity was kept constant to ensure consistent illumination. The entire set-up was placed on an active anti-vibration table (Halcyonics i4-large, Accurion, Germany) and contained in a closed box to minimize acoustic vibrations and to control the illumination conditions during the experiment.

One dataset consisted of 2^{15} monochromatic images of the cross-section of the micropipette cantilever recorded close to the end of the cantilever arm using a 40× objective and a high-speed camera at 400 fps (pco.edge 4.2, PCO, Germany). The relative shift of the micropipette position throughout the recording was determined using a cross-correlation analysis of the intensity profiles of the pipette cross-section, following established protocols [30,32]. The intensity profile was extracted from the centre line of each image. The profile of the first frame served as a reference for the correlation analysis against which the profiles of all subsequent images were correlated. Subtracting the position of the maximal correlation value in the auto-correlation of the reference profile from the position of the maximum of the cross-correlation of the reference profile with the intensity profiles in subsequent images gives the relative shift of the pipette position compared to the first frame. Interpolating the correlation curve using the Matlab function 'smoothingspline' over 40 pixels around the discrete maximal correlation value and extracting the shift corresponding to the maximum of the interpolation results in sub-pixel resolution.

6.4. Analysis of the power spectrum and noise

Following the Wiener–Khinchin theorem, we calculated the correlation of the noise in the range of 30–130 Hz from the power spectrum without a cell attached to the micropipette (shown in figure 2) using the inverse Fourier transform. As shown in electronic supplementary material, figure S6a, the correlation revealed a delta peak for zero shift only, i.e. the noise is uncorrelated in time as expected for white noise. Electronic supplementary material, figure S6b, displays the scatter of the Fourier coefficients of the same data. The Fourier coefficients were found to follow a Gaussian distribution for both real (see electronic supplementary material, figure S6c) and imaginary (see electronic supplementary material, figure S6d) parts centred around zero with finite variance. From this analysis, we conclude that the noise was white noise.

Assuming that the micropipette is a linear system, as is the Fourier transform, the white noise in the power spectrum can be accounted for with the offset d of the Gaussian fit as illustrated in equation (2.3). Due to linearity, each Fourier coefficient, represented as a signal vector, $\boldsymbol{s}$, in complex space, is constructed as the linear combination of a signal vector originating from the forcing of the cell, $\boldsymbol{c}$, and a noise signal vector $\boldsymbol{n}$. Following the law of cosines, the amplitude of the resulting signal vector, $|\boldsymbol{s}| = s$, can be calculated from the cell signal amplitude, c, and noise signal amplitude, n, as

$$s^2 = c^2 + n^2 - 2cn\ \cos(\alpha). \tag{6.1}$$

The phase α takes a random value since it is the combination of the phase of $\boldsymbol{c}$ and the phase of $\boldsymbol{n}$, the latter being random as discussed above. Averaging over multiple realizations yields

$$\langle s^2 \rangle = \langle c^2 \rangle + \langle n^2 \rangle - 2\langle cn\ \cos(\alpha) \rangle, \tag{6.2}$$

where '⟨⟩' indicates averaged quantities. Since the probability distribution of cos(α) is symmetric around zero, the last term cancels out. If the frequency sampling is sufficiently high, i.e. the frequency binning-width $\Delta f = f_{\mathrm{sample}}/N$ is small such that there is a large number of coefficients within a frequency interval over which the fitted frequency distribution changes significantly, fitting a distribution to the power spectrum is the same as locally averaging over many realizations. For a typical experiment in bulk conditions, the standard deviation of the Gaussian fit σ varied between 1 and 3 Hz, which was considerably larger than the frequency binning-width $\Delta f = 0.012$ Hz. Consequently, white noise was treated as a constant offset in the power spectrum, which has been subtracted in order to isolate the signal originating from the periodic forcing of the attached cell.

Data accessibility. All data supporting this study are shown in the figures of the paper and provided as electronic supplementary material, including micropipette deflection files for all experiments along with a Mathematica code to obtain and fit the micropipette frequency response function.

Authors' contributions. O.B. conceived the project. T.J.B. and O.B. designed the experiments. T.J.B. performed the experiments and analysed the data. T.J.B. and S.K. developed the dynamical model. T.J.B., C.T.K., Q.M. and O.B. developed the measurement protocol. T.J.B. wrote the first draft of the paper. All authors contributed to the preparation of the manuscript.

Competing interests. We declare we have no competing interests.

Funding. Funding was kindly provided by the Max Planck Society.

Acknowledgements. The authors are grateful to K. Dalnoki-Veress, K. Wan, B. Friedrich, H. Nobach and M. Lorenz for discussions. M. M. Makowski is acknowledged for technical assistance. The Göttingen Algae Culture Collection (SAG) kindly provided the *C. reinhardtii* wild-type strain SAG 11-32b.

References

1. Purcell EM. 1977 Life at low Reynolds number. *Am. J. Phys.* **45**, 3–11. (doi:10.1119/1.10903)
2. Berg HC. 1975 Bacterial behaviour. *Nature* **254**, 389–392. (doi:10.1038/254389a0)
3. Lauga E, Powers TR. 2009 The hydrodynamics of swimming microorganisms. *Rep. Prog. Phys.* **72**, 096601. (doi:10.1088/0034-4885/72/9/096601)
4. Berg HC, Brown DA. 1972 Chemotaxis in *Escherichia coli* analysed by three-dimensional tracking. *Nature* **239**, 500–504. (doi:10.1038/239500a0)
5. Alon U, Surette MG, Barbai N, Leibler S. 1999 Robustness in bacterial chemotaxis. *Nature* **397**, 168–171. (doi:10.1038/16483)
6. Foster KW, Saranak J, Patel N, Zarilli G, Okabe M, Kline T, Nakanishi K. 1984 A rhodopsin is the functional photoreceptor for phototaxis in the unicellular eukaryote *Chlamydomonas*. *Nature* **311**, 756–759. (doi:10.1038/311756a0)
7. Miki K, Clapham DE. 2013 Rheotaxis guides mammalian sperm. *Curr. Biol.* **23**, 443–452. (doi:10.1016/j.cub.2013.02.007)
8. Krieg M, Fläschner G, Alsteens D, Gaub BM, Roos WH, Wuite GJ, Gaub HE, Gerber C, Dufrêne YF, Müller DJ. 2019 Atomic force microscopy-based mechanobiology. *Nat. Rev. Phys.* **1**, 41–57. (doi:10.1038/s42254-018-0001-7)
9. Alsteens D, Gaub HE, Newton R, Pfreundschuh M, Gerber C, Müller DJ. 2017 Atomic force microscopy-based characterization and design of biointerfaces. *Nat. Rev. Mater.* **2**, 1–16. (doi:10.1038/natrevmats.2017.8)
10. Ashkin A, Dziedzic JM, Yamane T. 1987 Optical trapping and manipulation of single cells using infrared laser beams. *Nature* **330**, 769–771. (doi:10.1038/330769a0)
11. Min TL, Mears PJ, Chubiz LM, Rao CV, Golding I, Chemla YR. 2009 High-resolution, long-term characterization of bacterial motility using optical tweezers. *Nat. Methods* **6**, 831–835. (doi:10.1038/nmeth.1380)
12. Stellamanns E, Uppaluri S, Hochstetter A, Heddergott N, Engstler M, Pfohl T. 2014 Optical trapping reveals propulsion forces, power generation and motility efficiency of the unicellular parasites *Trypanosoma brucei brucei*. *Sci. Rep.* **4**, 6515. (doi:10.1038/srep06515)
13. Rüffer U, Nultsch W. 1985 High-speed cinematographic analysis of the movement of chlamydomonas. *Cell Motility* **5**, 251–263. (doi:10.1002/cm.970050307)
14. Minoura I, Kamiya R. 1995 Strikingly different propulsive forces generated by different dynein-deficient mutants in viscous media. *Cell Motil. Cytoskeleton* **31**, 130–139. (doi:10.1002/cm.970310205)
15. Polin M, Tuval I, Drescher K, Gollub JP, Goldstein RE. 2009 *Chlamydomonas* swims with two 'gears' in a eukaryotic version of run-and-tumble locomotion. *Science* **325**, 487–490. (doi:10.1126/science.1172667)
16. Guasto JS, Johnson KA, Gollub JP. 2010 Oscillatory flows induced by microorganisms swimming in two dimensions. *Phys. Rev. Lett.* **105**, 168102. (doi:10.1103/PhysRevLett.105.168102)
17. Ostapenko T, Schwarzendahl FJ, Böddeker TJ, Kreis CT, Cammann J, Mazza MG, Bäumchen O. 2018 Curvature-guided motility of microalgae in geometric confinement. *Phys. Rev. Lett.* **120**, 068002. (doi:10.1103/PhysRevLett.120.068002)
18. Brumley DR, Wan KY, Polin M, Goldstein RE. 2014 Flagellar synchronization through direct hydrodynamic interactions. *eLife* **3**, 02750. (doi:10.7554/eLife.02750)
19. Drescher K, Goldstein RE, Michel N, Polin M, Tuval I. 2010 Direct measurement of the flow field around swimming microorganisms. *Phys. Rev. Lett.* **105**, 168101. (doi:10.1103/PhysRevLett.105.168101)
20. Rüffer U, Nultsch W. 1987 Comparison of the beating of cis- and trans-flagella of *Chlamydomonas* cells held on micropipettes. *Cell Motil. Cytoskeleton* **7**, 87–93. (doi:10.1002/cm.970070111)
21. Bayly PV, Lewis BL, Ranz EC, Okamoto RJ, Pless RB, Dutcher SK. 2011 Propulsive forces on the flagellum during locomotion of *Chlamydomonas reinhardtii*. *Biophys. J.* **100**, 2716–2725. (doi:10.1016/j.bpj.2011.05.001)
22. Goldstein RE, Polin M, Tuval I. 2009 Noise and synchronization in pairs of beating eukaryotic flagella. *Phys. Rev. Lett.* **103**, 168103. (doi:10.1103/PhysRevLett.103.168103)
23. Wan KY, Goldstein RE. 2014 Rhythmicity, recurrence, and recovery of flagellar beating. *Phys. Rev. Lett.* **113**, 238103. (doi:10.1103/PhysRevLett.113.238103)
24. Wan KY, Leptos KC, Goldstein RE. 2014 Lag, lock, sync, slip: the many 'phases' of coupled flagella. *J. R. Soc. Interface* **11**, 20131160. (doi:10.1098/rsif.2013.1160)
25. Johnson RE, Brokaw CJ. 1979 Flagellar hydrodynamics. A comparison between resistive-force theory and slender-body theory. *Biophys. J.* **25**, 113-127. (doi:10.1016/S0006-3495(79)85281-9)
26. McCord RP, Yukich JN, Bernd KK. 2005 Analysis of force generation during flagellar assembly through optical trapping of free-swimming *Chlamydomonas reinhardtii*. *Cell Motil. Cytoskeleton* **61**, 137–144. (doi:10.1002/cm.20071)
27. Wan KY. 2018 Coordination of eukaryotic cilia and flagella. *Essays Biochem.* **62**, 829–838. (doi:10.1042/EBC20180029)
28. Kantsler V, Dunkel J, Polin M, Goldstein RE. 2013 Ciliary contact interactions dominate surface scattering of swimming eukaryotes. *Proc. Natl Acad. Sci. USA* **110**, 1187–1192. (doi:10.1073/pnas.1210548110)
29. Contino M, Lushi E, Tuval I, Kantsler V, Polin M. 2015 Microalgae scatter off solid surfaces by hydrodynamic and contact forces. *Phys. Rev. Lett.* **115**, 258102. (doi:10.1103/PhysRevLett.115.258102)
30. Kreis CT, Le Blay M, Linne C, Makowski MM, Bäumchen O. 2018 Adhesion of *Chlamydomonas* microalgae to surfaces is switchable by light. *Nat. Phys.* **14**, 45–49. (doi:10.1038/nphys4258)
31. Petit J, Thomi L, Schultze J, Makowski M, Negwer I, Koynov K, Herminghaus S, Wurm FR, Bäumchen O, Landfester K. 2018 A modular approach for multifunctional polymersomes with controlled adhesive properties. *Soft Matter* **14**, 894–900. (doi:10.1039/C7SM01885A)
32. Backholm M, Bäumchen O. 2019 Micropipette force sensors for *in vivo* force measurements on single cells and multicellular microorganisms. *Nat. Protoc.* **14**, 594–615. (doi:10.1038/s41596-018-0110-x)
33. Kreis CT, Grangier A, Bäumchen O. 2019 *In vivo* adhesion force measurements of *Chlamydomonas* on model substrates. *Soft Matter* **15**, 3027–3035. (doi:10.1039/C8SM02236D)
34. Colbert MJ, Raegen AN, Fradin C, Dalnoki-Veress K. 2009 Adhesion and membrane tension of single vesicles and living cells using a micropipette-based technique. *Eur. Phys. J. E* **30**, 117–121. (doi:10.1140/epje/i2009-10514-7)
35. Colbert MJ, Brochard-Wyart F, Fradin C, Dalnoki-Veress K. 2010 Squeezing and detachment of living cells. *Biophys. J.* **99**, 3555–3562. (doi:10.1016/j.bpj.2010.10.008)
36. Backholm M, Ryu WS, Dalnoki-Veress K. 2013 Viscoelastic properties of the nematode *Caenorhabditis elegans*, a self-similar, shear-thinning worm. *Proc. Natl Acad. Sci. USA* **110**, 4528–4533. (doi:10.1073/pnas.1219965110)

37. Schulman RD, Backholm M, Ryu WS, Dalnoki-Veress K. 2014 Dynamic force patterns of an undulatory microswimmer. *Phys. Rev. E* **89**, 050701. (doi:10.1103/PhysRevE.89.050701)
38. Schulman RD, Backholm M, Ryu WS, Dalnoki-Veress K. 2014 Undulatory microswimming near solid boundaries. *Phys. Fluids* **26**, 101902. (doi:10.1063/1.4897651)
39. Backholm M, Kasper AKS, Schulman RD, Ryu WS, Dalnoki-Veress K. 2015 The effects of viscosity on the undulatory swimming dynamics of *C. elegans*. *Phys. Fluids* **27**, 091901. (doi:10.1063/1.4931795)
40. Sader JE. 1998 Frequency response of cantilever beams immersed in viscous fluids with applications to the atomic force microscope. *J. Appl. Phys.* **84**, 64–76. (doi:10.1063/1.368002)
41. Geyer VF, Jülicher F, Howard J, Friedrich BM. 2013 Cell-body rocking is a dominant mechanism for flagellar synchronization in a swimming alga. *Proc. Natl Acad. Sci. USA* **110**, 18 058–18 063. (doi:10.1073/pnas.1300895110)
42. Williams RE, Hussey RG. 1972 Oscillating cylinders and the Stokes' paradox. *Phys. Fluids* **15**, 2083. (doi:10.1063/1.1693839)
43. Tuck EO. 1969 Calculation of unsteady flows due to small motions of cylinders in a viscous fluid. *J. Eng. Math.* **3**, 1–20. (doi:10.1007/BF01540826)